Three North African Dust Source Areas and their Geochemical Fingerprint

Amy M. Jewell[a]*, Nick Drake[b,c], Anya J. Crocker[a], Natalie L. Bakker[b], Tereza Kunkelova[a], Charlie S. Bristow[d], Matthew J. Cooper[a], J. Andrew Milton[a], Paul S. Breeze[b], Paul A. Wilson[a]

*Corresponding author email: amj1g13@soton.ac.uk

a) University of Southampton, National Oceanography Centre Southampton, Waterfront Campus, European Way, Southampton, SO14 3ZH, UK

b) Department of Geography, Bush House North East Wing, Kings College London, London, WC2B 4BG, UK

c) Department of Archaeology, Max Planck Institute for the Science of Human History, Jena, Kahlaische Strasse 10, D-07745, Germany.

d) Department of Earth and Planetary Sciences, Birkbeck University of London, Malet Street, London, WC1E 7HX, UK

Highlights

- We define three preferential source areas (PSAs) for North African dust.
- Our data show Nd and Sr isotopic distinction between PSAs.
- We find extreme geochemical heterogeneity in the Bodélé Depression region.
- We find grain size influences on Sr and Nd isotopes in immature geologic settings.

Abstract

North Africa produces more than half of the world's atmospheric dust load. Once entrained into the atmosphere, this dust poses a human health hazard locally. It also modifies the radiative budget regionally, and supplies nutrients that fuel primary productivity across the North Atlantic Ocean and as far afield as the Amazonian Basin. Dust accumulation in deep sea and lacustrine sediments also provides a means to study changes in palaeoclimate, particularly those associated with rainfall climate change. Systematic analysis of satellite imagery has greatly improved our understanding of the trajectories of long-range North African dust plumes, but our knowledge of the dust-producing source regions and our ability to fingerprint their contribution to these export routes is surprisingly limited. Here we report new radiogenic isotope (Sr and Nd) data for sediment samples from known dust-producing substrates (dried river and lakes beds), integrate them with published isotope data and weight them for dust source activation. We define three isotopically distinct preferential dust source areas (PSAs): a Western, a Central and an Eastern North African PSA. More data are needed, particularly from the Western PSA, but our results show a change in PSA dust source composition to more radiogenic Nd- and less radiogenic Sr-isotope values from west to east, in line with the overall decreasing age of the underlying bedrock. Our data reveal extreme isotopic heterogeneity within the Chadian region of the Central PSA, including an extremely distinctive geochemical fingerprint feeding the Bodélé Depression, the most active dust source on Earth. Our new analysis significantly improves the reliability by which windblown dust deposits can be geochemically fingerprinted to their distant source regions.

Keywords:

North Africa, dust source, Bodélé Depression, radiogenic isotopes, εNd, 87Sr/86Sr

1. Introduction

Atmospheric dust is a key component of Earth's climate system, influencing the global radiative budget both directly by controlling absorption and scattering of solar radiation, and indirectly by stimulating cloud condensation and cover (Thompson et al., 2019). Today, North Africa exports more dust to the atmosphere than any region on Earth with an estimated annual production of 170 to 1600 Tg yr^{-1} (Engelstaedter et al., 2006), over half the total global flux (Ginoux et al., 2012). In some regions, these loadings constitute a serious risk to human health; high concentrations of atmospheric particulate matter with an aerodynamic diameter of less than 2.5 μm ($PM_{2.5}$) are estimated to have led to between 194,000 and 709,000 infant deaths in North Africa in 2015 alone (Heft-Neal et al., 2018). Once lofted into the atmosphere, North African dust can be carried thousands of kilometres, primarily to the west, in plumes that are visible from space and are suggested to transport Fe and other fertilizing micronutrients to sites of primary production in the surface waters of the North Atlantic Ocean (Jickells, 2005) and the rainforests of the Amazonian Basin (Koren et al., 2006; Yu et al., 2015). The accumulation of this dust in marine or lacustrine sediments also provides a way to investigate past changes in climate variability on geological timescales (Cole et al., 2009; Grousset et al., 1998; Tiedemann et al., 1994).

Systematic analysis of satellite imagery has greatly improved our understanding of the generation and export of North African dust. Key developments include providing the spatial coverage to map the locations of highest dust generation (Engelstaedter et al., 2006;

Schepanski et al., 2012) and establishing that there are two main transport pathways westwards, a “northern route” towards the Caribbean which dominates during boreal summer, and a “southern route” towards the Amazon during winter (Engelstaedter et al., 2006; Meng et al., 2017). Yet despite these recent advances, major uncertainties remain in our knowledge of North African dust-producing source regions and our ability to fingerprint their contribution to these export routes (Bakker et al., 2019; Formenti et al., 2011; Scheuvens et al., 2013). This limited knowledge base hinders the development of a comprehensive source-to-sink understanding and adds uncertainty to climatic interpretations that rely on the accumulation of dust in geological archives.

The first studies employing satellite-derived data in North Africa inferred dust sources from high atmospheric dust loads using AI (Aerosol Index) or AOT (Aerosol Optical Thickness) data from the Total Ozone Mapping Spectrometer (TOMS) or Ozone Monitoring Instrument (OMI) (Engelstaedter et al., 2006; Israelevich et al., 2002; Middleton and Goudie, 2001; Prospero et al., 2002) (Figure 1A). These analyses provided an invaluable first-look at the problem but were limited by a daily temporal resolution that conflated dust emission and dust transport (Schepanski et al., 2012). More recent work has employed the thermal infra-red (IR) radiances dataset from the Meteosat Second Generation (MSG) Spinning Enhanced Visible and InfraRed Imager (SEVIRI) which benefits from a much higher temporal resolution (every 15 minutes versus every 24 hours for TOMS and OMI). This higher temporal resolution approach allows dust source activation events to be identified at hourly resolution and geo-located by manually tracking dust plumes back to their precise origin (Schepanski et al., 2012, 2007). The resulting dust source activation frequency (DSAF) maps therefore effectively remove transport bias altogether (Figure 1B).

Once defined geographically by remote sensing analysis, preferential source areas of dust generation (PSAs) are characterised geochemically to permit dust provenance studies (e.g., Figure 1C & 1D). The primary tools that have been used in this endeavour are the radiogenic isotope analysis (mainly ε_{Nd} and $^{87}Sr/^{86}Sr$) of bedrock and associated lithogenic sediments. Yet, there are two main problems associated with existing interpretations of this kind. First, previous landmark studies noted the disparity in dust sources identified by the different remote sensing techniques outlined above and combined the results of the these approaches to identify six PSAs in North Africa (Fig. 1C, Scheuvens et al., 2013). However, this approach incorporates residual transport bias in dust emission estimates (Schepanski et al., 2012, 2007). Second, a large fraction of the Sr and Nd isotope data set currently available does not come from active deflating dust source regions (Abouchami et al., 2013; Blanchet, 2019; Gross et al., 2016; Scheuvens et al., 2013; Zhao et al., 2018). Dust in North Africa is mostly derived from distinct palaeolake- and alluvial- deposits, which are located in the foothills of Saharan mountain ranges (Bakker et al., 2019; Schepanski et al., 2009). Surrounding bedrock and sand sediments contain very limited fine-grained material, which inhibits dust production from these surfaces (Bullard et al., 2011). While samples from bedrock and sand deposits in the vicinity of dust sources are useful for investigating local sediment dynamics, they are not well-suited to fingerprinting the signature of dust transported over thousands of kilometres. Moreover, existing radiogenic isotope data have been generated on differing grain size fractions, ranging from bulk sediment measurements to < 2 µm. While the Nd isotope composition of aeolian dust is considered insensitive to grain size, Sr isotope data are widely suggested to be susceptible to a substantial grain-size dependent fractionation (with an increase in $^{87}Sr/^{86}Sr$ of ~ 0.01 in the < 2 µm fraction

compared to the >50 µm fraction, (Feng et al., 2009). Here we address these issues in identifying the geochemical signature of exported dust by presenting new PSAs, geographically defined based on the dust source activation frequency (DSAF) map of Schepanski et al. (2012) and isotopically characterised using our new Sr and Nd data combined with existing datasets from known dust sources. Our overarching aim is to improve the reliability by which dust deposits can be geochemically fingerprinted to their distant source regions.

2. Materials and Methods

2.1 Geographical definition of PSAs using remotely sensed data

To identify dominant dust source areas in North Africa and to guide sampling, we used the DSAF map of Schepanski et al. (2012), generated using MSG SEVIRI thermal IR radiances (Figure 1B & Figure 2A). It is based on highly resolved data (temporal resolution of 1-hour, spatial resolution of 3 km x 3 km) collected from the geostationary MSG satellite, allowing dust source activation events to be identified and traced back to their point of origin (see Schepanski et al., (2007, 2012) for their methodological details). We used their 1 ° x 1 ° annual DSAF map of the region between 5 °N; 20 °W and 40 °N; 40 °E for from March 2006 to February 2010 (Schepanski et al., 2012) to select samples for geochemical characterisation of PSAs.

2.2 Dust samples

Our sample set consists of sediments from dried lake and river beds from identified dust source regions in Chad (specifically the Bodélé Depression, Ennedi Mountains, the Bahr El Gazel and Lake Fitri), Morocco (Wadi Draa in the Zagora and M'Hamid regions), Sudan

(Nubian Desert) and Mauritania (Sebkhet Chemchan) (Figure 2A). Samples were collected during field campaigns between 2005 and 2019 and details are listed in Table 1.

2.3 Radiogenic Isotope analysis

Radiogenic isotope (Sr and Nd) data were generated on 42 sediment samples. Of these, 32 samples were dry sieved to isolate the < 32 µm fraction. To investigate the influence of changing sediment grain size on Sr and Nd isotope composition, five samples were further sieved to separate the 63 - 45 µm, 45 - 32 µm, and < 32 µm fractions, and then passed through a dust chamber to separate the < 10 µm fraction. Bulk measurements were obtained from nine samples from nearby the Bodélé Depression in Chad, and one from Mauritania. All samples were decarbonated in excess 10% (v/v) acetic acid overnight on a shaker table. The carbonate-free fraction was then rinsed three times with MQ water.

Radiogenic isotope analyses were carried out in a clean chemistry laboratory at the University of Southampton Waterfront Campus, NOCS. Approximately 100 mg of decarbonated sample was digested overnight using a HF-HNO_3-$HClO_4$ acid mixture at 130 °C. The digestion blanks (i.e. acid residue after full digestion procedure with no sample) were below detection level (level of detection was 0.051 ppm & 0.266 ppm for Nd and Sr respectively, calculated by $\bar{x}_{blank} + 3\sigma$). Nd and Sr were isolated using chromatographic column separation (adapted from Bayon et al. (2002)). Nd was isolated using a cation column (Bio-Rad AG-50W-X8 resin) followed by a reverse phase column (Ln-spec resin) (Pin and Zalduegui, 1997). Sr was isolated using Sr-spec resin. The total column blanks (i.e. when

blank acid is run through the column procedure) were negligible (50 pg and 30 pg) compared to the total amounts analysed (1 µg and 200 ng) for Sr and Nd respectively.

Nd-isotope ratios were measured using a Thermo Scientific Neptune multi-collector inductively coupled plasma mass spectrometer (MC-ICP-MS). $^{143}Nd/^{144}Nd$ compositions were corrected following the method of Vance and Thirlwall (2002) through adjustment to a $^{146}Nd/^{144}Nd$ ratio of 0.7219 and a secondary normalisation to $^{142}Nd/^{144}Nd$ = 1.141876. Results for the JNdi-1 reference standard (Tanaka et al., 2000) measured as an unknown were 0.512115 with an external reproducibility of the ±0.000006 (2SD) across 6 analysis sessions over two years. For convenience $^{143}Nd/^{144}Nd$ is reported here in epsilon notation (ε_{Nd}), where $^{143}Nd/^{144}Nd_{CHUR}$ represents the Chondrite Uniform Reservoir value of 0.512638 (Jacobsen and Wasserburg, 1980):

$$\varepsilon_{Nd} = \left[\frac{{}^{143}Nd/{}^{144}Nd_{sample}}{{}^{143}Nd/{}^{144}Nd_{CHUR}} - 1 \right] \times 10^4$$

After column separation, the Sr fraction was dried down and loaded onto an outgassed tantalum filament with 1µl of a tantalum activator solution. The samples were analysed on a ThermoScientific Triton Plus Thermal Ionisation Mass Spectrometer (TIMS) using a multi-dynamic procedure with an ^{88}Sr intensity of 2V. Fractionation was corrected using an exponential correction normalised to $^{86}Sr/^{88}Sr$ = 0.1194. NIST987 (Yobregat et al., 2017) was run as a standard on each turret alongside our samples and was measured at 0.710241 ± 0.000013 (2SD) on 4 analyses. The long-term average for NIST987 on this instrument is

187 0.710243 ± 0.000020 (2SD) from 464 analyses. Rock standard JB-1a was run through the
188 same digestion and chemical separation procedures to give $^{87}Sr/^{86}Sr$ and ε_{Nd} values of
189 0.704112 ± 0.000014 (2SE) and 2.97 ± 0.17 (2SD) respectively (within accepted values,
190 GeoReM: Jochum et al., 2005)).
191
192 2.4 Generating geochemically representative PSA compositions
193 Our approach to geochemically defining PSA compositions differs in two important ways
194 from the previous studies. First, our PSA compositions are defined using only data from dust
195 producing substrates. We combined our new data with published data from dust-producing
196 substrates such as lacustrine and riverine sediments and soils, but excluded data from
197 bedrock and aerosol samples. Second, we applied a dust source activity weighting to the
198 isotope data. In the past, when geographically defined using remote sensing methods that
199 conflate dust deflation and transport, PSA signatures were defined using the ranges of
200 isotopic data generated on all samples that fall within those PSA regions, defining a "box" or
201 field in Sr-Nd space. While this simple method is a sensible first order approach, it has the
202 important limitation that equal weighting is given to all isotopic measurements, regardless
203 of the contribution of the substrate to atmospheric dust loading. We applied a weighting to
204 the isotope data according to annual DSAF (in each case the DSAF value from the
205 corresponding 1 ° x 1 ° square was used as a multiplier) (Schepanski et al., 2012). To reduce
206 bias caused by uneven sampling, where there are multiple samples available within one 1 ° x
207 1 ° square, the isotope data were averaged and the resulting value was weighted by DSAF.
208 The weighted mean isotopic signature for each PSA is calculated by:

209
$$\bar{x}_{PSA} = \frac{\sum(x_i \times w_i)}{\sum w_i}$$

211 $$where\ x_i = sample\ isotope\ signature, w_i = DSAF$$

210

212 The weighted mean standard deviation for each PSA is calculated by:

213 $$st.dev_{PSA} = \sqrt{\frac{\sum(w_i\ (x_i - \bar{x}_{PSA})^2)}{\frac{(N-1)\sum w_i}{N}}}$$

214 $$where\ x_i = sample\ isotope\ signature, w_i = DSAF,\ N = no.of\ samples$$

215 We also calculate the percentage coverage for each PSA (i.e. the proportion of 1 ° x 1 °

216 squares of DSAF **>** 0 % that have an isotopic value assigned).

217

218 **3. Results and Discussion**

219 3.1 PSA geomorphology

220 The distribution of DSAF in North Africa changes seasonally. For most of the year,

221 particularly in boreal summer when dust export is greatest (Engelstaedter and Washington,

222 2007) (Figure 2B), there are three main geographically distinct hotspots of dust source

223 activation (i) West Sahara/Sahel (Southern Algeria, North East Mali, West Niger, North

224 Mauritania), (ii) Central Sahara/Sahel (Chad) and (iii) East Sahara/Sahel (North Eastern

225 Sudan) (Schepanski et al., 2007), hereafter the Western, Central and Eastern source regions

226 (Figure 2C). These hotspots are separated by topographic highs; the Hoggar and Aïr

227 mountains between the Western and Central source regions, and the Ennedi Mountains

228 between the Central and Eastern sources (Figure 2C). Furthermore, the three dust source

229 regions are sufficiently distinct geographically to mean that they lie within separate palaeo

230 river catchment basins (Drake et al., 2011).

231

The most active dust sources in North Africa are desiccated river and lake beds (Prospero et al., 2002), contributing approximately 36% and 64% of total North African winter dust respectively (Bakker et al., 2019). The Western source region (Figure 2) is dominated by dust production from alluvial deposits and palaeolakes in the deserts that surround the Aïr and Adrar Iforas Mountains spanning Algeria, Mali and Niger. Similarly, in the Eastern source region (Figure 2), dust derives largely from alluvial deposits in the Nubian desert (Bakker et al., 2019). The Central source region is the most active of the PSAs, and its main contributor is the Bodélé Depression. The Bodélé Depression is often described as the "dustiest place on Earth" and is estimated to contribute 50% - 64% of all North African dust (Bakker et al., 2019; Bristow et al., 2009; Engelstaedter et al., 2006; Evan et al., 2015) because of the combination of strong near surface winds funnelled between the nearby Tibesti and Ennedi mountains, and the large reservoir of easily deflatable, low density diatomite-rich sediment (Bristow et al., 2009; Washington et al., 2006). DSAF data may even underestimate the importance of this region as a dust source due to its extremely high dust loadings over a small geographical area (Evan et al., 2015).

The Bodélé Depression is located within the palaeolake Megachad basin which, during its mid-Holocene high-stand, reached 360,000 km^2 in size (Figure 3) and 170 m in depth (Drake and Bristow, 2006). Modern day Lake Chad is located within the southern part of the palaeolake basin and covers only ~ 5% of its mid-Holocene area (Bristow et al., 2018) (Figure 3). The Bodélé Depression lies within the northern part of the basin and remains dry today, separated from modern-day Lake Chad by a 285-m-high sill. During humid intervals in the past when lake levels exceeded 285 m, water flowed from Lake Chad in the south to the Bodélé Depression in the north via a palaeoriver system known as the Bahr El Gazel (Figure

3). Today, exposed diatomites in the Bahr El Gazel also act as an important dust source, contributing ~10% of North African winter dust (Bakker et al., 2019). To the east of the Bodélé Depression, a palaeoriver system originating in the Ennedi, Wadi Fira, Quaddai and Sila provinces feeds into palaeolake Megachad. From north to south, these rivers are locally known as Ouadi Archei, Ouadi Chili, Ouadi Oum Hadjer, Ouadi Haouach, Ouadi Yedinga, Ouadi Haddad and Ouadi Enne, and hereafter collectively referred to as the Eastern palaeorivers. A palaeoriver system originating in the Tibesti mountains feeds in from the north west, of which the main rivers are known as Enneri Ké and Enneri Modragué. Today the alluvial deposits that remain from all of these palaeoriver systems are important dust sources.

3.2 PSA geochemical fingerprints

3.2.1 Three geochemically distinct PSAs

Regional bedrock geology can have a major impact on the isotopic signature of aeolian sediments. The three main dust source regions that we define in Figure 2 are located within differing geological settings (Begg et al., 2009; Van Hinsbergen et al., 2011). The Western source region is strongly influenced by the West African Craton where bedrocks are of Paleoproterozoic age. The Central source region is characterized by younger basement rocks of Neoproterozoic age, and the Saharan Metacraton. The Eastern source region is much younger geologically and characterised by outcropping basic volcanic rocks. However, surface sediments from dust generation hotspots may have already been transported thousands of kilometres from their bedrock sources by the action of winds or rivers, which can result in a smoothing of spatial heterogeneities in bedrock geology (Reynolds et al., 2006).

Here, we combine new and existing data from known dust-producing substrates to quantify the isotopic signature of material emitted from each of our three newly outlined PSAs. The data set that we present includes samples from locations with a wide range of dust source activation frequencies (Figure 4A, section 2.4). The extent to which the locations with the highest DSAF have been sampled is variable by PSA (Figure 4B-D) and some geographical regions of data sparsity are unavoidable (Figure 2A). Least well sampled is the Western PSA, especially in its central and south-eastern regions where political unrest has limited ground-access in recent years. Nevertheless, there is reasonable isotopic agreement between our weighted mean ε_{Nd} signature for the Western PSA and the ε_{Nd} of airborne trap samples of dust collected on the Senegalese coast, which was backtracked to Mauritania, Western Sahara and the hotspot between Mali, Niger and Algeria (Skonieczny et al., 2013), all within our Western PSA. This similarity suggests that our data provide a good first approximation of the Western PSA (Supp. Figure 1) but the mismatch in $^{87}Sr/^{86}Sr$ (approximately 0.01, Supp. Figure 1) suggests that more coverage is needed.

The data that we present indicate a clear isotopic distinction between the three PSAs (Table 2 & Figure 5). The Western source region has the most radiogenic weighted mean $^{87}Sr/^{86}Sr$ signature (0.72788 ± 0.00520 (1sd)) and the most unradiogenic ε_{Nd} signature (-14.79 ± 2.16 (1sd)). The Eastern source region has a weighted mean $^{87}Sr/^{86}Sr$ of 0.70580 ± 0.00142 (1sd) and ε_{Nd} of -1.34 ± 2.46 (1sd). The Central source region has a weighted mean $^{87}Sr/^{86}Sr$ of 0.71863 ± 0.00530 (1sd) and a weighted mean ε_{Nd} of -9.96 ± 3.85 (1sd), but is highly heterogeneous and is therefore discussed in detail in a separate section below (Section 3.2.2). These broad trends from west to east in $^{87}Sr/^{86}Sr$ (to less radiogenic values) and ε_{Nd}

304 (to more radiogenic values) are consistent with large-scale North African bedrock geology
305 which gets progressively younger from west to east (Begg et al., 2009; Van Hinsbergen et al.,
306 2011). This result shows that the mixing effects of dust transportation and deposition across
307 North African have a subordinate influence on regional isotope composition compared to
308 underlying geology at a continental scale. Compared to previous PSA isotopic definitions
309 (Abouchami et al., 2013; Pourmand et al., 2014; Scheuvens et al., 2013), weighting our data
310 by DSAF leads to less overlap between the isotopic signatures of our new PSAs, especially
311 between the Western and Central PSAs, permitting effective identification of source areas
312 from downwind sample analyses.
313
314 The Western source region is most active during boreal summer (Schepanski et al., 2007)
315 and dominates dust transport to the nearshore eastern subtropical Atlantic (Engelstaedter
316 and Washington, 2007; Meng et al., 2017). Data sparsity for the Western PSA are currently
317 limiting but based on the large-scale bedrock geology (Begg et al., 2009) we anticipate that,
318 as more data become available, it may be possible to distinguish Western Sahara and
319 Mauritania as separate PSAs. Nevertheless, even based on the data available, the Western
320 source region appears geochemically distinct from the other two North African PSAs (Figure
321 5). A key priority for future sampling is the high dust emission frequency region where the
322 borders of Algeria, Mali and Niger meet. Evan et al., (2015) report that this region is
323 responsible for producing up to 13% of North African dust emissions, making it the second
324 largest dust source on the continent, yet to our knowledge, no radiogenic isotope data
325 currently exist for this region (Figure 2A).
326

In the Eastern source region, our new data from alluvial sediments in the Nubian Desert align with existing data from Sudan. Compiled new and existing data (Figure 5) range from -7.5 to +3.2 in ε_{Nd}, and from 0.70405 to 0.71691 in $^{87}Sr/^{86}Sr$. Of our three newly defined PSAs, this Eastern region has the most radiogenic Nd and non-radiogenic Sr isotope signatures, resulting from deposits left by palaeorivers draining young rocks. Data from the Eastern source region are extremely consistent, especially in Sr. This region produces dust year-round, but production is greatest during boreal summer (Engelstaedter and Washington, 2007; Schepanski et al., 2007). Dust is primarily transported from the Eastern source region via north-westerly winds to the Arabian Peninsula and the northern Arabian Sea. Sudan is historically under-appreciated as a dust source, however, Bakker et al. (2019) show that this is an important region of dust production, generating approximately 7.5% of North African wintertime dust. Our isotopic characterisation of high dust-producing substrates such as desiccated river beds will allow an improved definition of the contribution of this North African dust source to the Arabian Sea. To better understand the significance of this eastward dust flux from northeast African over geological timescales, further work is required to isotopically fingerprint other potential dust sources to the Arabian Sea, particularly over the Arabian Peninsula and eastern Horn of Africa.

3.2.2 Isotopic characterisation of the Bodélé Depression and surrounding area

The Central source region has the highest dust production of our three PSAs and includes Earth's greatest single dust source, the Bodélé Depression. It is particularly important to fingerprint the contribution of the Bodélé Depression to North African dust plumes to better understand its role in fertilising the Amazon rainforest and modifying the global radiative budget. Yet that task has been a challenging one because, while some isotope data are

351 available from the wider region, the Central PSA is highly heterogeneous, with a broad
352 range of isotopic signatures (ε_{Nd} values between -16.3 and -2.42 and $^{87}Sr/^{86}Sr$ between
353 0.70968 and 0.73181, Figure 5) (Abouchami et al., 2013; Gross et al., 2016; Grousset and
354 Biscaye, 2005; Kumar et al., 2014), and very few data have been published from within the
355 Bodélé Depression itself. Here, we present new radiogenic data from the Bodélé Depression
356 and the surrounding river systems to better understand the origin and signature of the dust
357 exported from this region.
358
359 Our data from the region immediately surrounding the Bodélé Depression show extreme
360 isotopic heterogeneities, particularly in ε_{Nd}, that have not previously been documented
361 (Figures 5 & 6). Palaeohydrological reconstructions (Drake et al., 2011) indicate that, during
362 African humid periods of the last glacial cycle, the Bodélé Depression was fed by rivers
363 flowing from three different areas: the Tibesti Mountains, the region surrounding the
364 Ennedi Mountains (Eastern palaeorivers) and modern Lake Chad via the Bahr el Gazel
365 (Figures 3 and 6A). These three hinterlands have different geology and therefore provide
366 lithogenic material with very different isotopic signatures to the Bodélé Depression, as well
367 as acting directly as dust sources themselves (Bakker et al., 2019).
368
369 Samples taken north of the Bodélé Depression, in the Angamma Delta, near to the Tibesti
370 Mountains have highly radiogenic Nd and non-radiogenic Sr compositions (ε_{Nd}: -3.4 to -2.4,
371 $^{87}Sr/^{86}Sr$: 0.70968 to 0.71050). This is the first time that dust sources with such a radiogenic
372 Nd signature have been reported in the central Sahel/Sahara. The Tibesti Massif is volcanic
373 and younger than the surrounding basement. Isotopic measurements on samples from
374 Wadi Yebigue, a granitic pluton from within the Tibesti Massif, range from -6.01 to -1.83 in

375 ε_{Nd} (back-calculated from a crystallisation age of 550 Ma), and 0.7254 to 0.87549 in $^{87}Sr/^{86}Sr$
376 (Suayah et al., 2006). This provides a possible endmember from which alluvial sediments
377 sampled in the Angamma Delta, draining the Tibesti Mountains, have derived. While the ε_{Nd}
378 data fit well, the $^{87}Sr/^{86}Sr$ data of the Wadi Yebigue are far more radiogenic than those
379 measured in the Angamma Delta. It is unlikely that the Wadi Yebigue pluton is
380 representative of the entire catchment surrounding the Tibesti Massif, so more data are
381 required to fully constrain the isotopic endmember leading to highly radiogenic ε_{Nd} values at
382 the northern extremity of the Bodélé Depression.
383
384 Samples taken within the Eastern palaeo-river system, to the south of the Ennedi
385 Mountains, have very different signatures to those of the Angamma Delta, with ε_{Nd} values
386 between -14.2 and -11.6, and $^{87}Sr/^{86}Sr$ between 0.71530 and 0.72063. There are no isotope
387 data available from the highland source of these rivers, but they are likely well-
388 approximated by the data that we present from the Eastern palaeoriver sediments.
389 Furthermore, the consistency of the Eastern palaeoriver data in Nd-Sr space, across a large
390 geographic area covering several branches of the palaeo river system, implies that this
391 system stemmed from a single source, in this case a Precambrian basement with Lower
392 Palaeozoic sandstone (Wolff, 1964).
393
394 Samples taken from south of the Bodélé Depression, in the Bahr El Gazel palaeoriver
395 system, exhibit highly radiogenic $^{87}Sr/^{86}Sr$ (0.72054 to 0.73181) and comparatively
396 unradiogenic ε_{Nd} (-13.1 to -9.9). Reconstructions (Drake and Breeze, 2016) suggest that the
397 Bahr El Gazel flowed out of Lake Chad when water levels surpassed the 285m sill, carrying
398 sediment north into the Bodélé Depression. While samples from modern day Lake Chad are

very limited, the similarity between the signatures of Lake Chad (ε_{Nd} of -12.7; Grousset and Biscaye, (2005)) and the Bahr El Gazel support this reconstruction.

Samples taken from within the Bodélé Depression itself have ε_{Nd} values between -11.9 and -7.4, and $^{87}Sr/^{86}Sr$ between 0.71523 and 0.71858. This is more radiogenic in ε_{Nd} and more narrowly defined in $^{87}Sr/^{86}Sr$ than reported previously (Abouchami et al., 2013; Scheuvens et al., 2013). We find that the isotopic signature of the Bodélé Depression can be explained by mixing of the three isotopically distinct riverine endmembers (the Bahr El Gazel, Tibesti and Eastern palaeorivers) (Figure 6B), in line with palaeohydrological reconstructions (Drake et al., 2011). Several smaller palaeolakes (Figure 6B) located to the west of the Bodélé Depression exhibit isotopic values similar to it, indicating that they were also fed by a mixture of the Bahr El Gazel, and palaeorivers draining the Tibesti Mountains and Eastern highlands. This contrasts with samples from modern lakes south of the Bodélé Depression (Lake Fitri), which exhibit a different isotopic signature ($^{87}Sr/^{86}Sr$ of 0.72423, ε_{Nd} of -16.3 to -13.6, this study), indicating a different source of sediment to this locality.

The disparity between our isotopic definition of the Bodélé Depression and those previously reported (Abouchami et al., 2013; Scheuvens et al., 2013) primarily stems from differing naming protocols for samples from the Bodélé Depression and its surrounding geomorphological features. While several studies (Abouchami et al., 2013; Gross et al., 2016; Grousset and Biscaye, 2005; Kumar et al., 2014) sampled close to the Bodélé Depression, until our work (this study), data from samples taken from within the palaeolake basin were extremely sparse (Figure 6A). Many samples taken from nearby regions, several close to modern day Lake Chad, and others within the Bahr El Gazel, were originally

423 classified as “Bodélé” samples. Our data show that the term “Bodélé Depression” should be
424 reserved for the diatomite-rich palaeolake basin in the north of palaeolake Megachad.
425 Abouchami et al. (2013) distinguished between Si-rich and Ca-rich components of Chadian
426 dust sources, however the variability seen in Sr-Nd isotope space in their data is modest in
427 comparison to that documented for our sample set, most likely because their samples
428 spanned a smaller geographical range. Their Si-rich source is the diatomite-rich alluvial
429 deposits of the Bahr El Gazel whereas their Ca-rich source is a palaeolake bed neighbouring
430 the Bodélé Depression where the isotopic signature is very similar to that of our Eastern
431 palaeoriver endmember, indicating its primary source.
432
433 The Central PSA is an active dust source all year round, but most important during boreal
434 winter when the Western and Eastern PSAs become distinctly less active than in summer
435 (Ben-Ami et al., 2012; Schepanski et al., 2007). Dust from this region is transported via the
436 Harmattan Trade winds towards the Eastern Equatorial Atlantic and onwards to South
437 America (Meng et al., 2017). North African dust is hypothesised to have a significant
438 fertilising effect on the nutrient-poor soils of the Amazon rainforest (Yu et al., 2015). Our
439 radiogenic isotopic data will help to assess the role of the Bodélé Depression in this process.
440 Comparison of the isotopic signature of dust accumulating in marine sediment cores off the
441 North West African margin to the central dust source will help to evaluate the relative
442 contributions of dust sources and also shed light on the palaeo-history of the Bodélé
443 Depression and palaeolake Megachad.
444
445 3.2.3 Effect of grain size on Sr and Nd isotope signature

Sr and Nd isotope systems provide conservative fingerprints of PSAs over long geological timescales and geographical distances. Nd isotopes are not considered to fractionate isotopically during weathering or transport, so the isotopic signature is passed directly from source rock to sink (Feng et al., 2009; Goldstein et al., 1984; Meyer et al., 2011). Conversely, Sr isotopes are suggested to fractionate during weathering and transport processes, with several studies demonstrating increased $^{87}Sr/^{86}Sr$ with increasing weathering intensity and with decreasing grain size (Feng et al., 2009; Grousset et al., 1992; Meyer et al., 2011).

We analysed five samples from the Central Source region across four different size fractions: 63 - 45 μm, 45 - 32 μm, < 32 μm and <10 μm. Overall, the magnitude of variation evidenced in our samples due to changing grain size is small in comparison to isotopic differences between the newly defined PSAs. Yet, variability is documented in both Nd and Sr isotope composition with grain size (Figure 7), and the magnitude and sign of these signals varies by location.

We find minimal grain-size variability in ε_{Nd} and $^{87}Sr/^{86}Sr$ in the sample from the Bahr El Gazel (BEG2), and the sample from the Bodélé Depression (BOD1) shows only a modest increase in radiogenic ε_{Nd} values with decreasing grain size, with no significant change in $^{87}Sr/^{86}Sr$. Conversely, three samples from the Eastern palaeorivers (EN4, EN13, EN14) show more pronounced grain size variation but with no consistent sign of change in either ε_{Nd} and $^{87}Sr/^{86}Sr$. This result suggests that the sediments proximal to the Ennedi Highlands are immature and poorly sorted when compared to sediments in the Bodélé Depression and the Bahr El Gazel.

Although there appears to be a wide acceptance in the literature (e.g. Feng et al., 2009; Grousset et al., 1992; Meyer et al., 2011; Újvári et al., 2018) that Nd isotopes do not fractionate with increased weathering and decreasing grain size, this perception stems from data reported on only one or two samples (Goldstein et al., 1984; Grousset et al., 1998). Our results show that significant grain size effects can occur in both strontium and neodymium isotopes in chemically immature sediments, therefore highlighting the need for more detailed research to better understand the extent to which sediment grain size can influence Nd isotopes in different geological settings, and how the isotopic signature of sediment evolves with transport history. It is important to isolate one consistent grain size fraction when analysing sediment for Sr and Nd isotope composition. Alternatively, work is needed to establish the scale of isotopic variability with varying grain size in the study region, especially when working with chemically immature sediments.

4. Conclusions

We identify three readily discernible North African dust PSAs, defined geographically using a high resolution Dust Source Activation Frequency map (Schepanski et al., 2012) and characterised geochemically using Sr and Nd isotopes (Figure 8). We weight geochemical data by locality dust source activation to produce representative estimates of the isotopic signature of emitted dust. The Western Source area is characterised by the most unradiogenic Nd and most radiogenic Sr signature, reflecting the old cratonic bedrock geology. More work is needed to validate the isotopic signatures of the major sites of dust activation in this understudied region, particularly targeting the alluvial sediments in Southern Algeria, Eastern Mali and North West Niger. The historically underestimated Eastern source region is geochemically well defined, and shows radiogenic Nd and non-

494 radiogenic Sr values. The Central dust source region is highly geochemically heterogenous.
495 We find that the isotopic signature of the Bodélé Depression is the result of mixing from
496 three geochemically distinct palaeo-river systems: the Bahr El Gazel, and rivers draining
497 from the Tibesti Mountains and Eastern highlands. We identify a strong grain-size effect on
498 the Nd and Sr isotopic signature of the immature Eastern palaeoriver sediments in
499 particular, highlighting the need to determine the nature and importance of grain size
500 effects in a specific study region.
501
502 Our new characterisation of North African dust source regions provides distinct fingerprints
503 to facilitate analysis of downwind dust trap samples, and help determine the role of specific
504 dust sources in fertilising North Atlantic surface waters and the Amazon rainforest during
505 different seasons (Kumar et al., 2018; Yu et al., 2015). Our data set also provides a
506 framework to establish changes in the contribution of different continental dust source
507 regions on geological timescales, through comparison to downcore records preserved in
508 marine and lacustrine sediments, and to help to shed new light on the history of palaeolake
509 Megachad. On finer spatial scales, the improved understanding of the isotopic signature of
510 the region surrounding the Bodélé Depression corroborates palaeo river drainage
511 reconstructions (Drake et al., 2011). Our study demonstrates the importance of
512 understanding the geomorphological context of dust source regions in order to accurately
513 define them geochemically, and highlights where future sampling should be focussed to
514 further improve the geochemical characterisation of North African dust sources.
515

Acknowledgements

This work was supported by the Natural Environment Research Council [grant number NE/L002531/1 to AMJ and NE/L002485/1 to NLB] and Royal Society Challenge Grant CH160073 and Royal Society Wolfson Merit Award to PAW. Research by PSB and ND utilised in this paper was funded by the Leverhulme Trust (grants RPG-2016-115 & ECF-2019-538). We thank Prof. Zongbo Shi and Clarissa Baldo from the University of Birmingham and Thomas Baird from University College London for their kind assistance. We are indebted to Dr. Moussa Abderamane from the University of N'Djamena and Dr Ahmed Adam from the University of Khartoum for their help arranging fieldwork and sample permits.

Reference List

Abouchami, W., Näthe, K., Kumar, A., Galer, S.J.G., Jochum, K.P., Williams, E., Horbe, A.M.C., Rosa, J.W.C., Balsam, W., Adams, D., Mezger, K., Andreae, M.O., 2013. Geochemical and isotopic characterization of the bodélé depression dust source and implications for transatlantic dust transport to the Amazon basin. Earth Planet. Sci. Lett. 380, 112–123. https://doi.org/10.1016/j.epsl.2013.08.028

Armitage, S.J., Bristow, C.S., Drake, N.A., 2015. West African monsoon dynamics inferred from abrupt fluctuations of Lake Mega-Chad. Proc. Natl. Acad. Sci. 112, 8543–8548. https://doi.org/10.1073/pnas.1417655112

Bakker, N.L., Drake, N.A., Bristow, C.S., 2019. Evaluating the Relative Importance of African Mineral Dust Sources Using Remote Sensing. Atmos. Chem. Phys. 19, 10525–10535.

Bayon, G., German, C.R., Boella, R.M., Milton, J.A., Taylor, R.N., Nesbitt, R.W., 2002. An improved method for extracting marine sediment fractions and its application to Sr and Nd isotopic analysis. Chem. Geol. 187, 179–199. https://doi.org/10.1016/S0009-2541(01)00416-8

Begg, G.C., Griffin, W.L., Natapov, L.M., O'Reilly, S.Y., Grand, S.P., O'Neill, C.J., Hronsky, J.M.A., Djomani, Y.P., Swain, C.J., Deen, T., Bowden, P., 2009. The lithospheric architecture of Africa: Seismic tomography, mantle petrology, and tectonic evolution. Geosphere 5, 23–50. https://doi.org/10.1130/GES00179.1

Ben-Ami, Y., Koren, I., Altaratz, O., Kostinski, A., Lehahn, Y., 2012. Discernible rhythm in the spatio/temporal distributions of transatlantic dust. Atmos. Chem. Phys. 12, 2253–2262. https://doi.org/10.5194/acp-12-2253-2012

Blanchet, C.L., 2019. A database of marine and terrestrial radiogenic Nd and Sr isotopes for tracing earth-surface processes. Earth Syst. Sci. Data 11, 742–759. https://doi.org/10.5194/essd-2018-109

Bristow, C.S., Drake, N., Armitage, S., 2009. Deflation in the dustiest place on Earth: The Bodélé Depression, Chad. Geomorphology 105, 50–58. https://doi.org/10.1016/j.geomorph.2007.12.014

Bristow, C.S., Holmes, J.A., Mattey, D., Salzmann, U., Sloane, H.J., 2018. A late Holocene palaeoenvironmental 'snapshot' of the Angamma Delta, Lake Megachad at the end of the African Humid Period. Quat. Sci. Rev. 202, 182–196. https://doi.org/10.1016/j.quascirev.2018.04.025

Bullard, J.E., Harrison, S.P., Baddock, M.C., Drake, N., Gill, T.E., McTainsh, G., Sun, Y., 2011.

564 Preferential dust sources: A geomorphological classification designed for use in global
565 dust-cycle models. J. Geophys. Res. Earth Surf. 116.
566 https://doi.org/10.1029/2011JF002061
567 Cole, J.M., Goldstein, S.L., DeMenocal, P.B., Hemming, S.R., Grousset, F.E., 2009. Contrasting
568 compositions of Saharan dust in the eastern Atlantic Ocean during the last deglaciation
569 and African Humid Period. Earth Planet. Sci. Lett. 278, 257–266.
570 https://doi.org/10.1016/j.epsl.2008.12.011
571 Drake, N., Breeze, P., 2016. Climate Change and Modern Human Occupation of the Sahara
572 from MIS 6-2, in: Africa from MI6-2. pp. 103–122. https://doi.org/10.1007/978-94-017-
573 7520-5
574 Drake, N., Bristow, C., 2006. Shorelines in the Sahara: Geomorphological evidence for an
575 enhanced monsoon from palaeolake Megachad. Holocene 16, 901–911.
576 https://doi.org/10.1191/0959683606hol981rr
577 Drake, N.A., Blench, R.M., Armitage, S.J., Bristow, C.S., White, K.H., 2011. Ancient
578 watercourses and biogeography of the Sahara explain the peopling of the desert. Proc.
579 Natl. Acad. Sci. https://doi.org/10.1073/pnas.1012231108
580 Engelstaedter, S., Tegen, I., Washington, R., 2006. North African dust emissions and
581 transport. Earth-Science Rev. 79, 73–100.
582 https://doi.org/10.1016/j.earscirev.2006.06.004
583 Engelstaedter, S., Washington, R., 2007. Atmospheric controls on the annual cycle of North
584 African dust. J. Geophys. Res. Atmos. 112. https://doi.org/10.1029/2006JD007195
585 Evan, A.T., Fiedler, S., Zhao, C., Menut, L., Schepanski, K., Flamant, C., Doherty, O., 2015.
586 Derivation of an observation-based map of North African dust emission. Aeolian Res.
587 16, 153–162. https://doi.org/10.1016/j.aeolia.2015.01.001

588 Feng, J.L., Zhu, L.P., X.L., Z., Hu, Z.G., 2009. Grain size effect on Sr and Nd isotopic
589 compositions in eolian dust : Geochem. J. 43, 123–131.
590 Formenti, P., Schütz, L., Balkanski, Y., Desboeufs, K., Ebert, M., Kandler, K., Petzold, A.,
591 Scheuvens, D., Weinbruch, S., Zhang, D., 2011. Recent progress in understanding
592 physical and chemical properties of African and Asian mineral dust. Atmos. Chem. Phys.
593 11, 8231–8256. https://doi.org/10.5194/acp-11-8231-2011
594 Ginoux, P., Prospero, J.M., Gill, T.E., Hsu, N.C., Zhao, M., 2012. Global-scale attribution of
595 anthropogenic and natural dust sources and their emission rates based on MODIS Deep
596 Blue aerosol products. Rev. Geophys. 50, 1–36.
597 https://doi.org/10.1029/2012RG000388
598 Goldstein, S.L., O'nions, R.K., Hamilton, P.J., 1984. A Sm-Nd isotopic study of atmospheric
599 dusts and particulates from major river systems. Earth Planet. Sci. Lett. 70, 221–236.
600 Gross, A., Palchan, D., Krom, M.D., Angert, A., 2016. Elemental and isotopic composition of
601 surface soils from key Saharan dust sources. Chem. Geol. 442, 54–61.
602 https://doi.org/10.1016/j.chemgeo.2016.09.001
603 Grousset, F., Rognon, P., Coudé-Gaussen, G., Pédemay, P., 1992. Origins of peri-Saharan
604 dust deposits traced by their Nd and Sr isotopic composition. Palaeogeogr.
605 Palaeoclimatol. Palaeoecol. 93, 203–212. https://doi.org/10.1016/0031-
606 0182(92)90097-O
607 Grousset, F.E., Biscaye, P.E., 2005. Tracing dust sources and transport patterns using Sr, Nd
608 and Pb isotopes. Chem. Geol. https://doi.org/10.1016/j.chemgeo.2005.05.006
609 Grousset, F.E., Parra, M., Bory, A., Martinez, P., Bertrand, P., Shimmield, G., Ellam, R.M.,
610 1998. Saharan Wind Regimes Traced by the Sr-Nd Isotopic Composition of Subtropical
611 Atlantic Sediments: Last Glacial Maximum vs Today. Quat. Sci. Rev. 17, 395–409.

612 Heft-Neal, S., Burney, J., Bendavid, E., Burke, M., 2018. Robust relationship between air
613 quality and infant mortality in Africa. Nature 559, 254–258.
614 https://doi.org/10.1038/s41586-018-0263-3
615 Israelevich, P.L., Levin, Z., Joseph, J.H., Ganor, E., 2002. Desert aerosol transport in the
616 Mediterranean region as inferred from the TOMS aerosol index. J. Geophys. Res.
617 Atmos. 107. https://doi.org/10.1029/2001JD002011
618 Jacobsen, S.B., Wasserburg, G.J., 1980. Sm-Nd isotopic evolution of chondrites. Earth Planet.
619 Sci. Lett. 50, 139–155. https://doi.org/10.1016/0012-821X(80)90125-9
620 Jickells, T.D., 2005. Global Iron Connections Between Desert Dust, Ocean Biogeochemistry,
621 and Climate. Science (80-.). 308, 67–71. https://doi.org/10.1126/science.1105959
622 Jochum, K.P., Nohl, U., Herwig, K., Lammel, E., Stoll, B., Hofmann, A.W., 2005. GeoReM: A
623 new geochemical database for reference materials and isotopic standards. Geostand.
624 Geoanalytical Res. 29, 333–338. https://doi.org/10.1111/j.1751-908x.2005.tb00904.x
625 Koren, I., Kaufman, Y.J., Washington, R., Todd, M.C., Rudich, Y., Martins, J.V., Rosenfeld, D.,
626 2006. The Bodélé depression: A single spot in the Sahara that provides most of the
627 mineral dust to the Amazon forest. Environ. Res. Lett. 1. https://doi.org/10.1088/1748-
628 9326/1/1/014005
629 Kumar, A., Abouchami, W., Galer, S.J.G., Garrison, V.H., Williams, E., Andreae, M.O., 2014. A
630 radiogenic isotope tracer study of transatlantic dust transport from Africa to the
631 Caribbean. Atmos. Environ. 82, 130–143.
632 https://doi.org/10.1016/j.atmosenv.2013.10.021
633 Kumar, A., Abouchami, W., Galer, S.J.G., Pal, S., Fomba, K.W., Prospero, J.M., Andreae, M.O.,
634 2018. Seasonal radiogenic isotopic variability of the African dust outflow to the tropical
635 Atlantic Ocean and across to the Caribbean. Earth Planet. Sci. Lett. 487, 94–105.

636 https://doi.org/10.1016/j.epsl.2018.01.025
637 Meng, L., Gaao, H.W., Yu, Y., Gao, Y., Zhang, C., Fan, L., 2017. A new approach developed to
638 study variability in North African dust trans- port routes over the Atlantic during 2001–
639 2015. Geophys. Res. Lett. 44, 10,026-10,035. https://doi.org/10.1002/2017GL074478
640 Meyer, I., Davies, G.R., Stuut, J.B.W., 2011. Grain size control on Sr-Nd isotope provenance
641 studies and impact on paleoclimate reconstructions: An example from deep-sea
642 sediments offshore NW Africa. Geochemistry, Geophys. Geosystems 12.
643 https://doi.org/10.1029/2010GC003355
644 Middleton, N.J., Goudie, A.S., 2001. Saharan dust: Sources and trajectories. Trans. Inst. Br.
645 Geogr. 26, 165–181. https://doi.org/10.1111/1475-5661.00013
646 Padoan, M., Garzanti, E., Harlavan, Y., Villa, I.M., 2011. Tracing Nile sediment sources by Sr
647 and Nd isotope signatures (Uganda, Ethiopia, Sudan). Geochim. Cosmochim. Acta 75,
648 3627–3644. https://doi.org/10.1016/j.gca.2011.03.042
649 Pin, C., Zalduegui, J.F.S., 1997. Sequential separation of light rare-earth elements , thorium
650 and uranium by miniaturized extraction chromatography : Application to isotopic
651 analyses of silicate rocks. Anal. Chim. Acta 339, 79–89.
652 Pourmand, A., Prospero, J.M., Sharifi, A., 2014. Geochemical fingerprinting of trans-Atlantic
653 African dust based on radiogenic Sr-Nd-Hf isotopes and rare earth element anomalies.
654 Geology 42, 675–678. https://doi.org/10.1130/G35624.1
655 Prospero, J.M., Ginoux, P., Torres, O., Nicholson, S.E., Gill, T.E., 2002. Environmental
656 characterization of global sources of atmospheric soil dust identified with the Nimbus 7
657 Total Ozone Mapping Spectrometer (TOMS) absorbing aerosol product. Rev. Geophys.
658 40, 1–31. https://doi.org/10.1029/2000RG000095
659 Reynolds, R.L., Reheis, M., Yount, J., Lamothe, P., 2006. Composition of aeolian dust in

660 natural traps on isolated surfaces of the central Mojave Desert - Insights to mixing,
661 sources, and nutrient inputs. J. Arid Environ. 66, 42–61.
662 https://doi.org/10.1016/j.jaridenv.2005.06.031
663 Schepanski, K., Tegen, I., Laurent, B., Heinold, B., Macke, A., 2007. A new Saharan dust
664 source activation frequency map derived from MSG-SEVIRI IR-channels. Geophys. Res.
665 Lett. 34, 1–5. https://doi.org/10.1029/2007GL030168
666 Schepanski, K., Tegen, I., Macke, A., 2012. Comparison of satellite based observations of
667 Saharan dust source areas. Remote Sens. Environ. 123, 90–97.
668 https://doi.org/10.1016/j.rse.2012.03.019
669 Schepanski, K., Tegen, I., Todd, M.C., Heinold, B., Bönisch, G., Laurent, B., Macke, A., 2009.
670 Meteorological processes forcing Saharan dust emission inferred from MSG-SEVIRI
671 observations of subdaily dust source activation and numerical models. J. Geophys. Res.
672 Atmos. 114. https://doi.org/10.1029/2008JD010325
673 Scheuvens, D., Schütz, L., Kandler, K., Ebert, M., Weinbruch, S., 2013. Bulk composition of
674 northern African dust and its source sediments - A compilation. Earth-Science Rev.
675 https://doi.org/10.1016/j.earscirev.2012.08.005
676 Skonieczny, C., Bory, A., Bout-Roumazeilles, V., Abouchami, W., Galer, S.J.G., Crosta, X.,
677 Diallo, A., Ndiaye, T., 2013. A three-year time series of mineral dust deposits on the
678 West African margin: sedimentological and geochemical signatures and implications for
679 interpretation of marine paleo-dust records. Earth Planet. Sci. Lett. 364, 145–156.
680 Suayah, I.B., Miller, J.S., Miller, B. V, Bayer, T.M., Rogers, J.J.W., 2006. Tectonic significance
681 of Late Neoproterozoic granites from the Tibesti massif in southern Libya inferred from
682 Sr and Nd isotopes and U – Pb zircon data. J. African Earth Sci. 44, 561–570.
683 https://doi.org/10.1016/j.jafrearsci.2005.11.020

684 Tanaka, T., Togashi, S., Kamioka, H., Amakawa, H., Kagami, H., Hamamoto, T., Yuhara, M.,
685 Orihashi, Y., Yoneda, S., Shimizu, H., Kunimaru, T., Takahashi, K., Yanagi, T., Nakano, T.,
686 Fujimaki, H., Shinjo, R., Asahara, Y., Tanimizu, M., Dragusanu, C., 2000. JNdi-1: A
687 neodymium isotopic reference in consistency with LaJolla neodymium. Chem. Geol.
688 168, 279–281. https://doi.org/10.1016/S0009-2541(00)00198-4
689 Thompson, A.J., Skinner, C.B., Poulsen, C.J., Zhu, J., 2019. Modulation of Mid-Holocene
690 African Rainfall by Dust Aerosol Direct and Indirect Effects. Geophys. Res. Lett. 46,
691 3917–3926. https://doi.org/10.1029/2018GL081225
692 Tiedemann, R., Sarnthein, M., Shackleton, N.J., 1994. Astronomic timescale for the Pliocene
693 Atlantic d180 and dust flux records of Ocean Drilling Program site 659.
694 Paleoceanography 9, 619–638.
695 Újvári, G., Wegner, W., Klötzli, U., Horschinegg, M., Hippler, D., 2018. Sr-Nd-Hf Isotopic
696 Analysis of <10 mg Dust Samples: Implications for Ice Core Dust Source Fingerprinting.
697 Geochemistry, Geophys. Geosystems 19, 60–72.
698 https://doi.org/10.1002/2017GC007136
699 van der Does, M., Knippertz, P., Zschenderlein, P., Giles Harrison, R., Stuut, J.B.W., 2018. The
700 mysterious long-range transport of giant mineral dust particles. Sci. Adv. 4.
701 https://doi.org/10.1126/sciadv.aau2768
702 Van Hinsbergen, D.J.J., Buiter, S.J.H., Torsvik, T.H., Gaina, C., Webb, S.J., 2011. The formation
703 and evolution of Africa from the Archaean to present: Introduction. Geol. Soc. Spec.
704 Publ. 357, 1–8. https://doi.org/10.1144/SP357.1
705 Vance, D., Thirlwall, M., 2002. An assessment of mass discrimination in MC-ICPMS using Nd
706 isotopes. Chem. Geol. 185, 227–240. https://doi.org/10.1016/S0009-2541(01)00402-8
707 Washington, R., Todd, M.C., Lizcano, G., Tegen, I., Flamant, C., Koren, I., Ginoux, P.,

Engelstaedter, S., Bristow, C.S., Zender, C.S., Goudie, A.S., Warren, A., Prospero, J.M., 2006. Links between topography, wind, deflation, lakes and dust: The case of the Bodélé Depression, Chad. Geophys. Res. Lett. 33, 1–4. https://doi.org/10.1029/2006GL025827

Wolff, J.-P., 1964. Carte géologique de la République du Tchad.

Yobregat, E., Fitoussi, C., Bourdon, B., 2017. A new method for TIMS high precision analysis of Ba and Sr isotopes for cosmochemical studies. J. Anal. At. Spectrom. 32, 1388–1399. https://doi.org/10.1039/c7ja00012j

Yu, H., Chin, M., Yuan, T., Bian, H., Remer, L.A., Prospero, J.M., Omar, A., Winker, D., Yang, Y., Zhang, Y., Zhang, Z., Zhao, C., 2015. The fertilizing role of African dust in the Amazon rainforest: A first multiyear assessment based on data from Cloud-Aerosol Lidar and Infrared Pathfinder Satellite Observations. Geophys. Res. Lett. 42, 1984–1991. https://doi.org/10.1002/2015GL063040

Zhao, W., Balsam, W., Williams, E., Long, X., Ji, J., 2018. Sr–Nd–Hf isotopic fingerprinting of transatlantic dust derived from North Africa. Earth Planet. Sci. Lett. 486, 23–31. https://doi.org/10.1016/j.epsl.2018.01.004

Table Captions:

Table 1: New sample information. Samples marked with * were measured at 63 - 45 µm, 45 - 32 µm, <32 µm and <10 µm (BEG = Bahr El Gazel).

Table 2: Weighted mean (and weighted standard deviation) isotopic signatures of North African PSAs.

Figure Captions:

Figure 1: Previous analyses of North African preferential dust source areas (PSAs). 1 ° x 1 ° maps of North African dust sources from March 2006 to February 2010, based on A) OMI aerosol index (Map adapted from Schepanski et al., 2012; frequency-based remote sensing method) B) MSG SEVIRI IR dust index (Adapted from Schepanski, *et al*., 2012; employs backtracking method therefore removing dust transport bias). C) Geographical definition of North African Potential Source Areas (PSAs) of (Adapted from Scheuvens et al., 2013) based on a variety of remote sensing techniques that conflate dust transport and emission. D) Geochemical characterisation of North African PSAs, as defined in Figure 1C, in Nd-Sr isotope space (PSAs 1 - 4 & 6 as defined by Scheuvens et al., 2013, PSA 5 from Abouchami et al., 2013).

Figure 2: A new analysis revealing three North African preferential dust source areas (PSAs, this study). A) Annual dust source activation frequency (DSAF) (Schepanski et al., 2012) and location of existing (white circles) and new (red circles, this study) dust source samples with Sr and/or Nd isotope data (published data from Abouchami et al., 2013; Gross et al., 2016; Grousset et al., 1998; Kumar et al., 2014; Padoan et al., 2011; Zhao et al., 2018) . B) DSAF in boreal summer (JJA) (Schepanski et al., 2007). C) Three new PSAs (this study) based on the data in (A) and the

757 topographic highs used to separate them. Coloured shading denotes annual DSAF > 5 % (bold) and
758 DSAF < 5% (pale).
759
760 **Figure 3: Location, areal extent and palaeohydrology of palaeolake Megachad** (adapted from
761 Armitage et al., 2015).
762
763 **Figure 4: Distribution of dust source activation frequency (DSAF) and isotopic data coverage.**
764 Histograms showing the total area (i.e. number of 1 ° x 1 ° squares) covered by each DSAF bracket
765 (bold colours, Schepanski et al., 2012) and the corresponding area characterised by isotopic data
766 (pale bars, this study) for A) the whole of North Africa and for the B) Western, C) Central and D)
767 Eastern PSAs. Percentage coverage shown above each bar.
768
769 **Figure 5: Isotopic composition of our three North African PSAs.** New data (squares, this study) and
770 published data (circles) (Abouchami et al., 2013; Gross et al., 2016; Grousset et al., 1998; Kumar et
771 al., 2014; Padoan et al., 2011; Zhao et al., 2018) from North African dust source regions. Size
772 corresponds to annual DSAF (Schepanski et al., 2012). Crosses denote mean isotopic values for each
773 source region weighted by annual DSAF +/- one weighted standard deviation. Where only ε_{Nd} or
774 $^{87}Sr/^{86}Sr$ data is available, sample is not plotted, but the available data still contribute to the
775 weighted PSA mean.
776
777
778 **Figure 6: The Chadian region of the central preferential dust source area.** A) Sampling locations for
779 new data (squares, this study) and published data (circles, Abouchami et al., 2013; Gross et al., 2016;
780 Grousset and Biscaye, 2005; Kumar et al., 2014) from Chad, in the central PSA. Satellite image taken
781 from Google Earth, overlain with palaeo river reconstructions (Drake and Breeze, 2016). B) Sr and Nd
782 isotope data from Chad, in the Central PSA. Shading highlights main contributors determining the

783 isotopic signature of the Bodélé Depression (red): the Tibesti (orange), Eastern (green) and Bahr El
784 Gazel (yellow) palaeorivers. Smaller palaeolakes (lilac) are also likely fed by a mixture of these
785 palaeorivers.
786
787 **Figure 7: Effect of grain size on Sr and Nd isotopes within the central dust source region.** Symbol
788 size denotes grain size (63 - 45 µm, 45 – 32 µm, <32 µm and <10 µm). One sample from each of the
789 Bodélé (BOD1, red) and Bahr El Gazel (BEG2, yellow), and three from the Eastern palaeorivers (EN4,
790 EN13, EN14, green) were analysed. Sample locations shown in Figure 6. Black bars show 2 standard
791 error (often smaller than the symbol). $^{87}Sr/^{86}Sr$ for sample BEG2 < 10 µm did not successfully run, but
792 the ε_{Nd} is -12.26.
793
794 **Figure 8: $^{87}Sr/^{86}Sr$ (top) and ε_{Nd} (bottom) isotope composition of our three North African PSAs**
795 **(mean values, +/- 1sd, weighted by activation frequency of the source**. Dust sources (1 ° x 1 °) with
796 activation frequency > 5% (Schepanski et al., 2012) shown in bold colours, < 5% in pale colours.
797

Table 1

Central Source

Sample ID	Country	Location	Longitude (dec. degrees)	Latitude (dec. degrees)	Size fraction (µm)
34BOT25	Chad	Bodélé	18.466	16.914	Bulk
BOD1	Chad	Bodélé	18.467	16.916	<32 *
CH17	Chad	Bodélé	18.544	16.880	<32
CH34	Chad	Tibesti	17.671	17.508	Bulk
CH38	Chad	Tibesti	17.603	17.615	Bulk
CH39	Chad	Tibesti	17.603	17.615	Bulk
CH50	Chad	Bodélé	17.778	16.677	Bulk
CH56	Chad	Bodélé	17.639	16.864	Bulk
CH62	Chad	BEG	18.028	16.684	Bulk
CH75	Chad	BEG	18.271	15.758	Bulk
BEG1	Chad	BEG	18.610	15.777	<32
BEG2	Chad	BEG	18.560	15.726	<32 *
BEG3	Chad	BEG	18.512	15.698	<32
EN1	Chad	Ennedi	20.737	14.868	<32
EN2	Chad	Ennedi	20.619	15.227	<32
EN3	Chad	Ennedi	20.719	15.644	<32
EN4	Chad	Ennedi	21.137	16.347	<32 *
EN5	Chad	Ennedi	21.274	16.472	<32
EN6	Chad	Ennedi	21.623	16.733	<32
EN7	Chad	Ennedi	21.624	16.735	<32
EN8	Chad	Ennedi	21.714	16.828	<32
EN9	Chad	Ennedi	21.627	16.833	<32
EN12	Chad	Ennedi	21.606	16.834	<32
EN13	Chad	Ennedi	21.464	16.851	<32 *
EN14	Chad	Ennedi	21.081	16.158	<32 *
EN15	Chad	Ennedi	20.670	15.732	<32
RIVER1	Chad	Lake Fitri	17.652	12.869	<32
RIVER2	Chad	Lake Fitri	17.635	12.852	<32

Western Source

Sample ID	Country	Location	Longitude	Latitude	Size fraction (µm)
MauriLake	Mauritania	Sebkhet	-12.189	21.080	Bulk
MHAMID18	Morocco	M'Hamid	-5.699	29.795	<32
MHAMID19	Morocco	M'Hamid	-5.720	29.823	<32
ZAG1	Morocco	Zagora	-5.833	30.321	<32
ZAG2	Morocco	Zagora	-6.168	30.601	<32

Eastern Source

Sample ID	Country	Location	Longitude	Latitude	Size fraction (µm)
SD1	Sudan	Nubian Desert	33.976	19.796	<32
SD2	Sudan	Nubian Desert	33.999	19.817	<32
SD3	Sudan	Nubian Desert	34.762	20.139	<32
SD4	Sudan	Nubian Desert	36.099	21.457	<32
SD6	Sudan	Nubian Desert	36.154	20.693	<32
SD7	Sudan	Nubian Desert	34.811	19.940	<32
SD8	Sudan	Nubian Desert	34.669	19.740	<32
SD9	Sudan	Nubian Desert	34.549	19.386	<32
SD10	Sudan	Nubian Desert	34.440	19.119	<32

Table 2

	$^{87}Sr/^{86}Sr$	1 sd	ε_{Nd}	1 sd
Western	0.7279	0.0052	-14.79	2.16
Central	0.7186	0.0053	-9.96	3.85
Eastern	0.7058	0.0014	-1.34	2.46

Figure 1

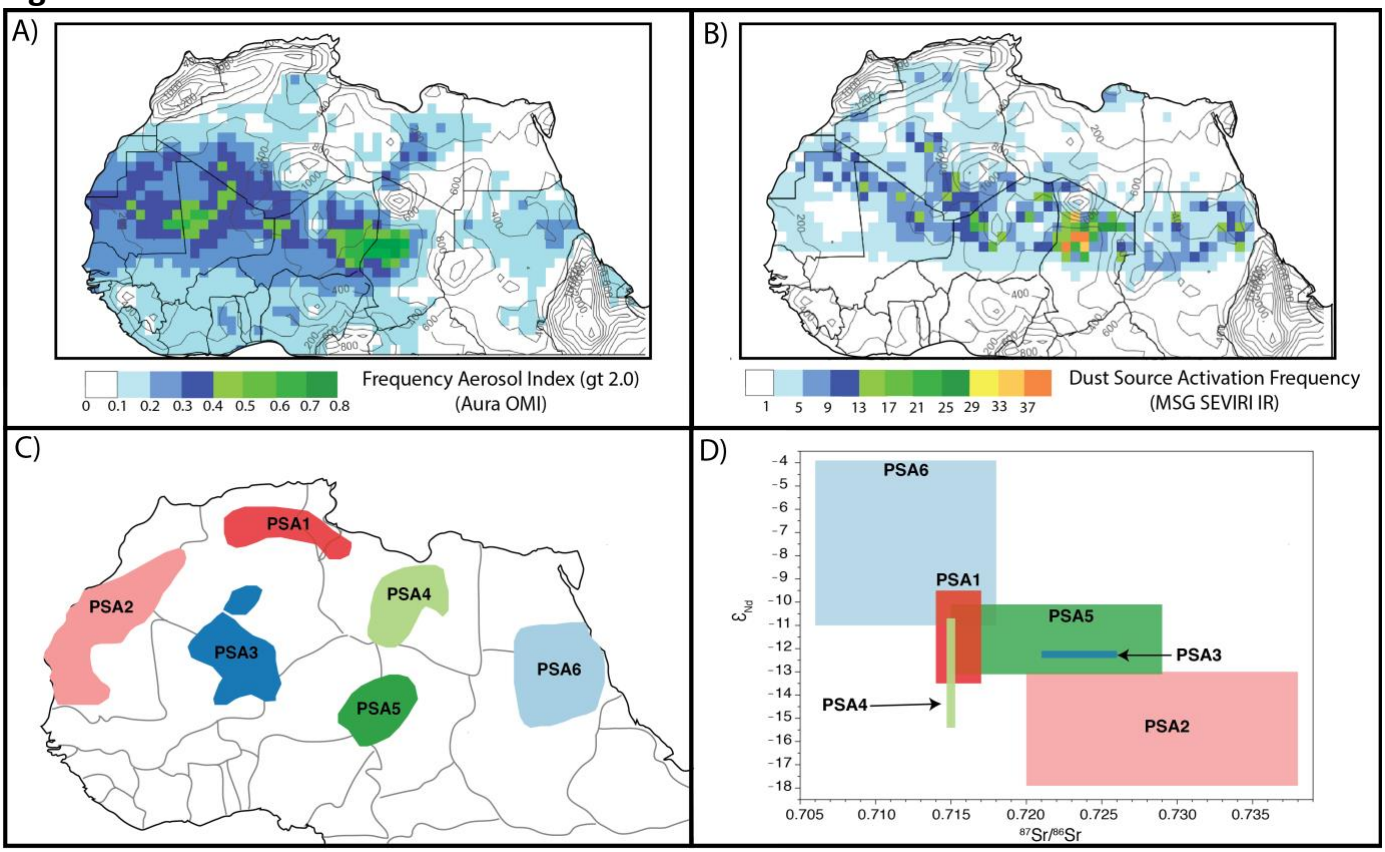
A)
0 0.1 0.2 0.3 0.4 0.5 0.6 0.7 0.8
Frequency Aerosol Index (gt 2.0)
(Aura OMI)
B)
1 5 9 13 17 21 25 29 33 37
Dust Source Activation Frequency
(MSG SEVIRI IR)
C)
PSA1
PSA2
PSA3
PSA4
PSA5
PSA6
D)
PSA6
PSA1
PSA5
PSA3
PSA4
PSA2
ε_{Nd}
$^{87}Sr/^{86}Sr$

Figure 2

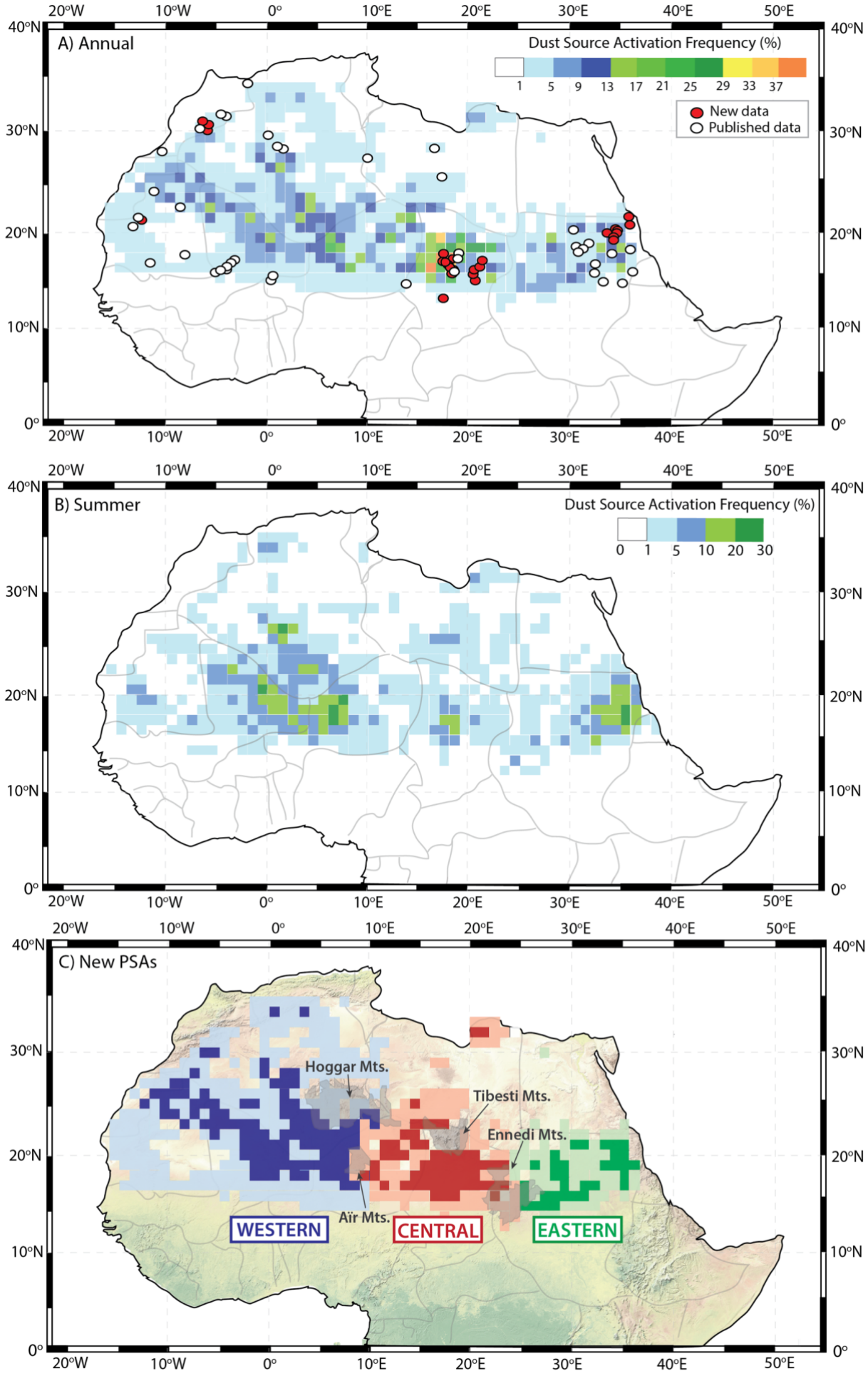
A) Annual
Dust Source Activation Frequency (%)
1 5 9 13 17 21 25 29 33 37
New data
Published data
B) Summer
Dust Source Activation Frequency (%)
0 1 5 10 20 30
C) New PSAs
Hoggar Mts.
Tibesti Mts.
Ennedi Mts.
Aïr Mts.
WESTERN
CENTRAL
EASTERN
20°W 10°W 0° 10°E 20°E 30°E 40°E 50°E
40°N 30°N 20°N 10°N 0°

Figure 3

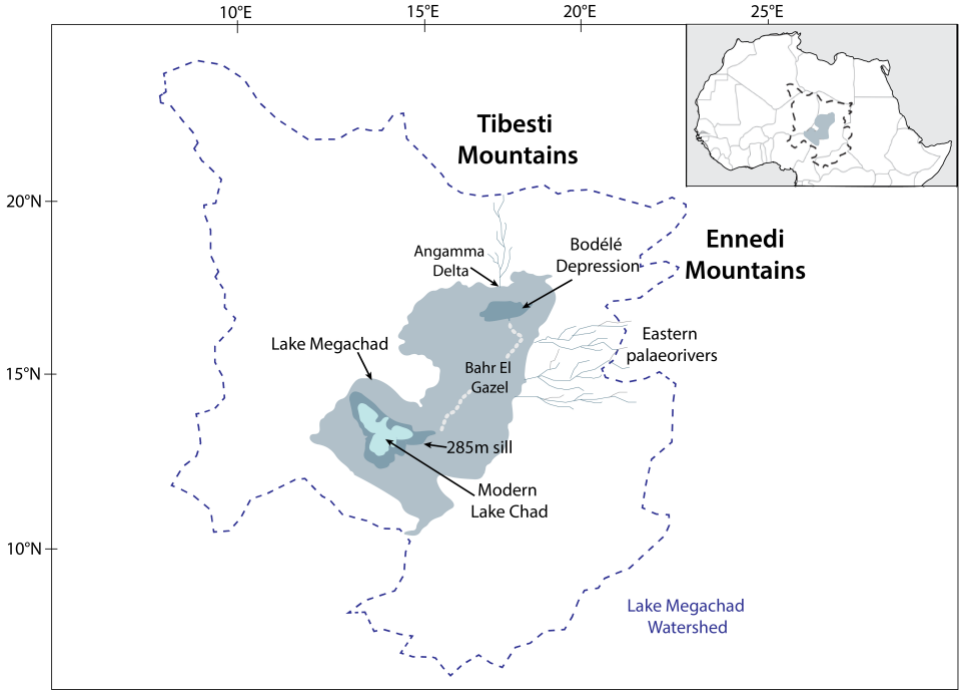

Figure 4

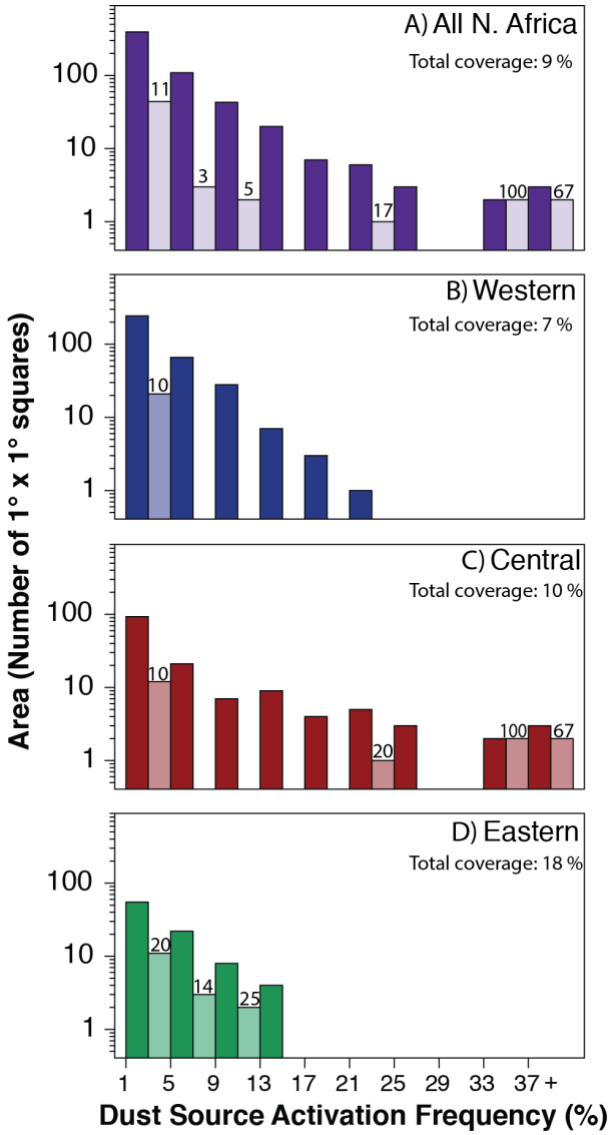

Figure 5

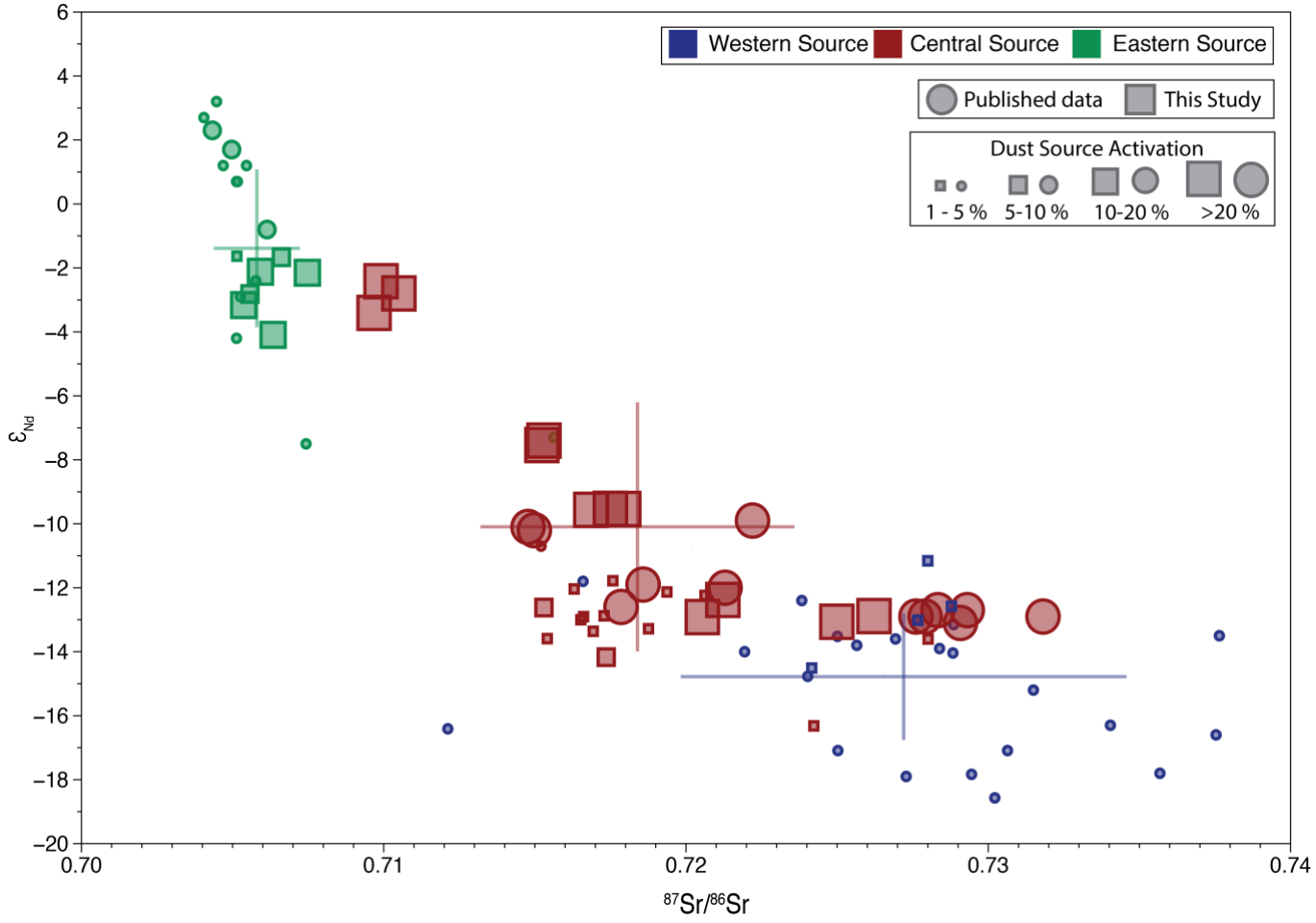

Figure 6

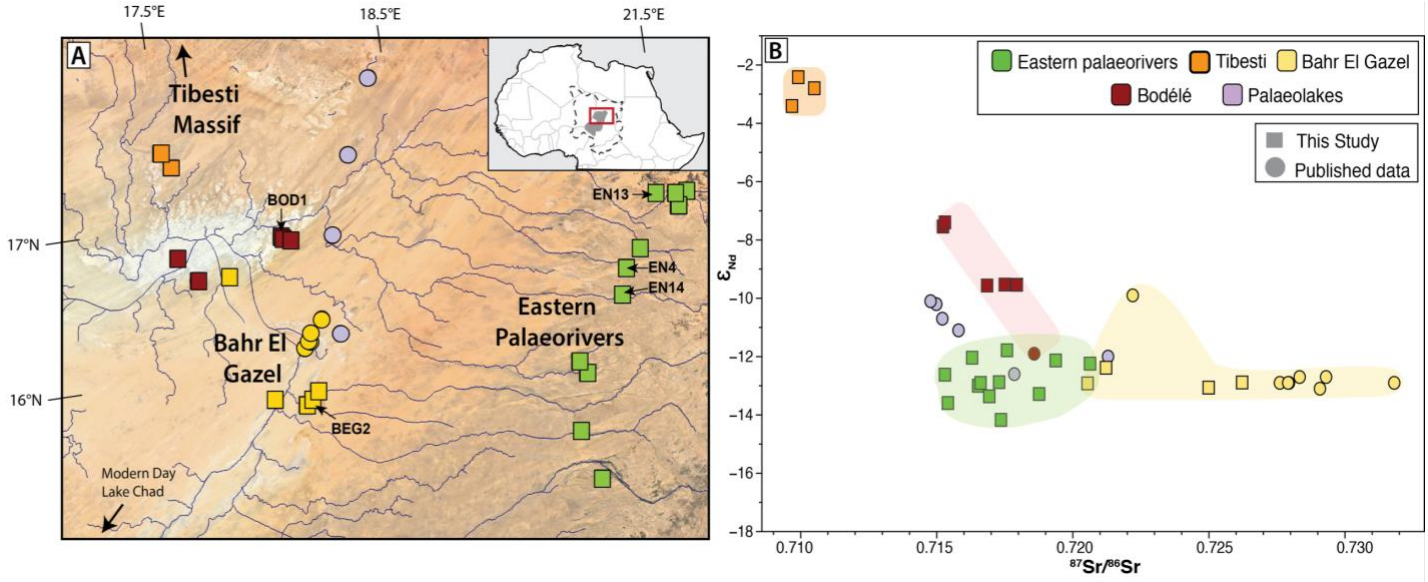

Figure 7

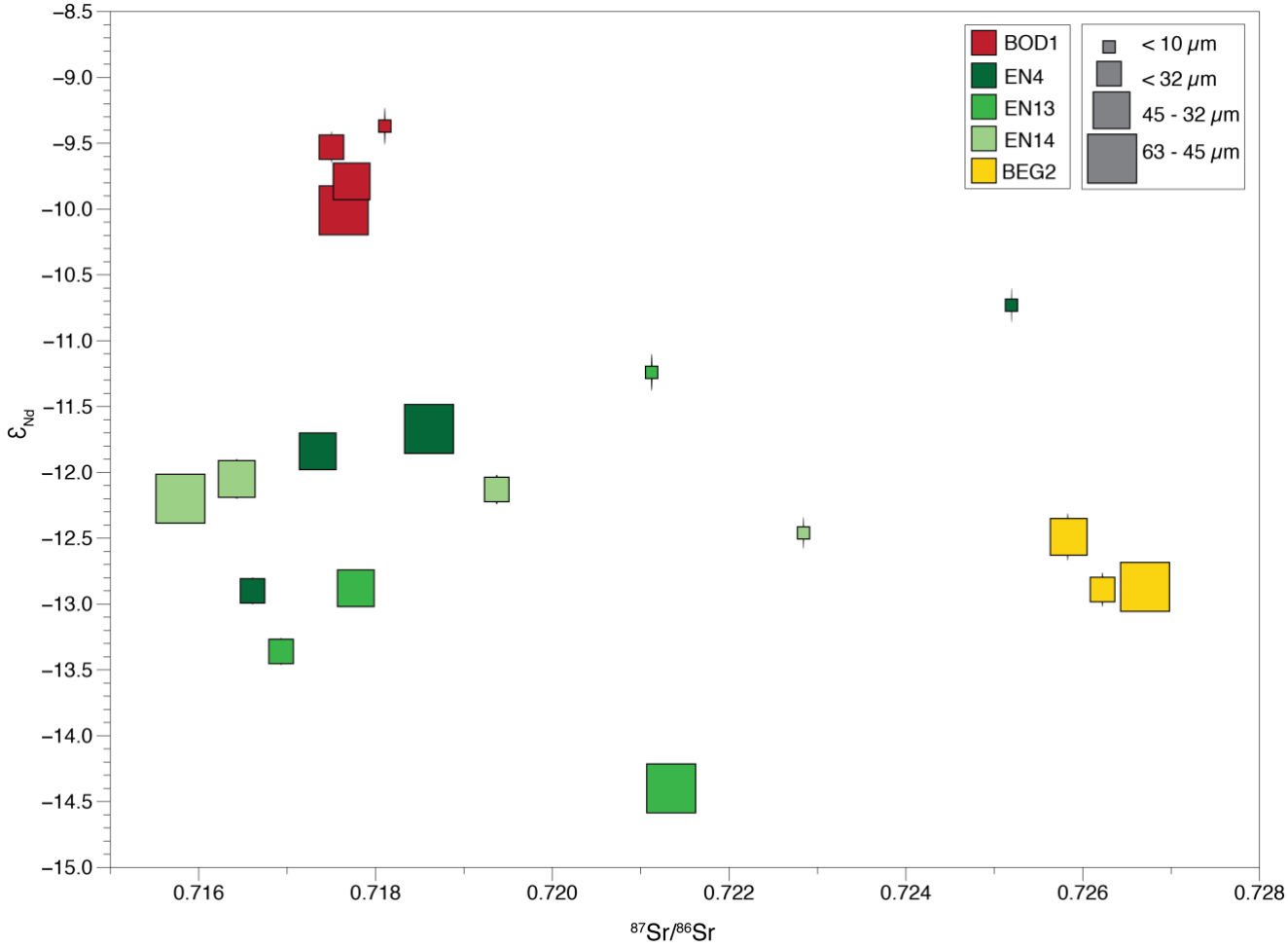

Figure 8